



# Correlated geophysical, geochemical, and volcanological manifestations of plume-ridge interaction along the Galápagos Spreading Center

**R. S. Detrick**

*Department of Geology and Geophysics, Woods Hole Oceanographic Institution, Woods Hole, Massachusetts 02543, USA (rdetrick@whoi.edu)*

**J. M. Sinton**

*School of Ocean and Earth Science and Technology, University of Hawaii, 2525 Correa Road, Honolulu, Hawaii 96822, USA (sinton@soest.hawaii.edu)*

**G. Ito**

*School of Ocean and Earth Science and Technology, University of Hawaii, 2525 Correa Road, Honolulu, Hawaii 96822, USA (gito@soest.hawaii.edu)*

**J. P. Canales**

*Department of Geology and Geophysics, Woods Hole Oceanographic Institution, Woods Hole, Massachusetts 02543, USA (jpcanales@whoi.edu)*

**M. Behn**

*MIT-WHOI Joint Program in Oceanography, Woods Hole Oceanographic Institution, Woods Hole, Massachusetts 02543, USA (mbehn@whoi.edu)*

**T. Blacic**

*Department of Geology, University of California, Davis, Davis, California 95616, USA (blacic@geology.ucdavis.edu)*

**B. Cushman**

*School of Ocean and Earth Science and Technology, University of Hawaii, 2525 Correa Road, Honolulu, Hawaii 96822, USA (bcushman@soest.hawaii.edu)*

**J. E. Dixon**

*Rosenstiel School of Marine and Atmospheric Sciences, University of Miami, Miami, Florida 33149, USA (jdixon@rsmas.miami.edu)*

**D. W. Graham**

*College of Oceanic and Atmospheric Sciences, Oregon State University, Corvallis, Oregon 97331, USA (dgraham@coas.oregonstate.edu)*

**J. J. Mahoney**

*School of Ocean and Earth Science and Technology, University of Hawaii, 2525 Correa Road, Honolulu, Hawaii 96822, USA (jmahoney@soest.hawaii.edu)*

[1] As the Galápagos hot spot is approached from the west along the Galápagos Spreading Center there are systematic increases in crustal thickness and in the K/Ti, Nb/Zr,  $^3\text{He}/^4\text{He}$ ,  $\text{H}_2\text{O}$ , and  $\text{Na}_2\text{O}$  content of lavas recovered from the spreading axis. These increases correlate with progressive transitions from rift valley to axial high morphology along with decreases in average swell depth, residual mantle Bouguer gravity



anomaly, magma chamber depth, average lava Mg #, Ca/Al ratio, and the frequency of point-fed versus fissure-fed volcanism. Magma chamber depth and axial morphology display a “threshold” effect in which small changes in magma supply result in large changes in these variables. These correlated variations in geophysical, geochemical, and volcanological manifestations of plume-ridge interaction along the western Galápagos Spreading Center reflect the combined effects of changes in mantle temperature and source composition on melt generation processes, and the consequences of these variations on magma supply, axial thermal structure, basalt chemistry, and styles of volcanism.

**Components:** 6355 words, 4 figures, 1 table.

**Keywords:** Mantle plumes; mid-ocean ridges; hotspots.

**Index Terms:** 8121 Tectonophysics: Dynamics, convection currents and mantle plumes; 7220 Seismology: Oceanic crust; 7218 Seismology: Lithosphere and upper mantle.

**Received** 25 March 2002; **Revised** 18 June 2002; **Accepted** 21 June 2002; **Published** 10 October 2002.

Detrick, R. S., J. M. Sinton, G. Ito, J. P. Canales, M. Behn, T. Blacic, B. Cushman, J. E. Dixon, D. W. Graham, and J. J. Mahoney, Correlated geophysical, geochemical, and volcanological manifestations of plume-ridge interaction along the Galápagos Spreading Center, *Geochem. Geophys. Geosyst.*, 3(10), 8501, doi:10.1029/2002GC000350, 2002.

**Theme:** Plume-Ridge Interaction

**Guest Editor:** David Graham

## 1. Introduction

[2] A significant portion of the global mid-ocean ridge system is influenced by mantle plumes [Schilling, 1991; Ito and Lin, 1995a]. Characterizing the distinctive gradients in geophysical and geochemical anomalies along plume-influenced ridges can help elucidate mantle processes such as mantle flow, source mixing, decompression melting, and melt migration in ways that are not possible along more “normal” ridge systems. Hot spot-related variations in magma production rates at a more or less constant spreading rate can also be used to examine the influence of magma supply on a wide range of crustal accretion processes, including the formation of axial topography, magma chamber properties, and style of volcanism. In this report we describe results from a combined geophysical and petrological investigation of an ~800-km-long section of the hot spot-influenced western Galápagos Spreading Center (GSC) that provides new insight into the effects of changes in mantle temperature and source composition on melt generation processes and the consequences of these variations on crustal accretion processes.

## 2. G-PRIME Experiment

[3] The east-west striking GSC separates the Cocos and Nazca plates in the eastern equatorial Pacific (Figure 1). The GSC is an intermediate spreading-rate ridge with full opening rates increasing from 45 mm/yr at 98°W to ~56 mm/yr at 91°W [DeMets *et al.*, 1990]. At 91°W the GSC lies ~200 km north of the Galápagos Archipelago, the western end of which marks the probable center of the Galápagos mantle plume [White *et al.*, 1993; Toomey *et al.*, 2001]. The proximity of the Galápagos hot spot has had a strong influence on the GSC. This can be seen in along-axis variations in bathymetry and gravity [Ito and Lin, 1995b], axial morphology [Canales *et al.*, 1997], in the chemical and isotopic composition of GSC basalts [Schilling *et al.*, 1976, 1982; Fisk *et al.*, 1982; Verma and Schilling, 1982; Verma *et al.*, 1983], and in the long history of rift propagation along the GSC [Hey, 1977; Wilson and Hey, 1995].

[4] In April–May 2000 the Galápagos Plume-Ridge Interaction Multidisciplinary Experiment (G-PRIME) conducted an extensive geophysical

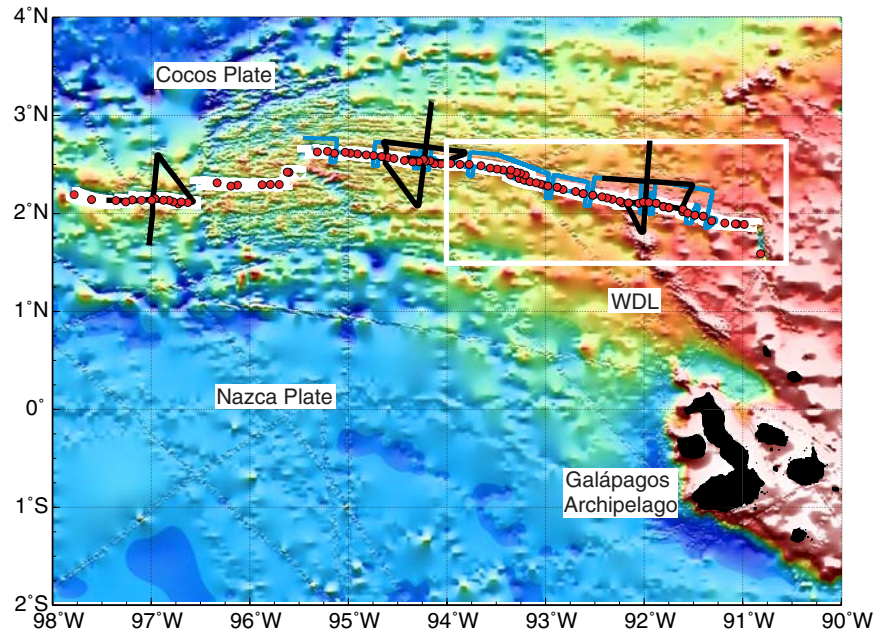


**Figure 1.** Map of the western Galápagos Spreading Center (GSC) and Galápagos swell based on integration of available multibeam bathymetry [Canales *et al.*, 1997; Hey *et al.*, 1992; this study] and satellite-derived seafloor topography data [Smith and Sandwell, 1997]. Water depths range from >3500 m (blue) to <1000 m (red). The axis of the east-west trending, intermediate-spreading rate GSC is shown by the thin white band. At 91°W, the GSC lies ~200 km north of the Galápagos Archipelago, the western end of which marks the probable center of the Galápagos mantle plume [White *et al.*, 1993; Toomey *et al.*, 2001]. The Galápagos swell is apparent in a gradual shoaling of sea floor depths along the western GSC over a distance of ~800 km. The Wolf-Darwin lineament (WDL) is a volcanic chain located on the southern flank of the GSC. Location of seismic refraction (black) and multichannel reflection (blue) lines, and lava sampling stations (red circles) obtained on the G-PRIME expedition are shown. White box indicates location of bathymetry map detail shown in Figure 3a.

and petrological investigation of the western GSC between 90.5°W and 98°W (Figure 1). The first modern multibeam bathymetry data were collected along the GSC between 90.5°W and 93.3°W, and west of 95°W, defining the location of the spreading axis and constraining the variation in axial morphology. In order to determine the thickness and internal structure of the crust, ~1400 km of multichannel seismic reflection data were obtained along the GSC between 91.25°W and 95°W, and three wide-angle seismic refraction experiments were carried out along parts of the GSC with distinctly different axial morphologies (rift valley, transitional morphology, and axial high).

[5] With the tectonic and structural context provided by these geophysical surveys, rock samples were collected at 91 stations along the GSC

between 90.5°W and 98°W, supplementing previous collections along the GSC between 83°W and 101°W [Schilling *et al.*, 1976, 1982] and near 95°W [Christie and Sinton, 1981, 1986; Hey *et al.*, 1992], to provide comprehensive petrological, geochemical, and He, Sr, Nd, and Pb isotopic data on lava compositions. Major and minor element abundances on these samples presented in this paper are University of Hawaii electron microprobe analyses of natural glasses; Nb/Zr was determined by X-ray fluorescence on whole rock samples at the University of Hawaii. Forty-five individual glasses were analyzed for dissolved H<sub>2</sub>O and CO<sub>2</sub> by Fourier transform spectrometer (FTIR) at the University of Miami. Thirty-six basalt glass samples were analyzed for <sup>3</sup>He/<sup>4</sup>He at Oregon State University. All geochemical data presented in this paper are summarized in Table 1.



**Table 1.** Galápagos Spreading Center: Glass and Whole Rock Data<sup>a</sup> [The full Table 1 is available in the HTML version of the article at <http://www.g-cubed.org>.]

Glass label	MORB-type	Glass Data										Whole Rock Data				
		Longitude, °W	Mg#	K/Ti	Na8.0	Ca8.0/A18.0	H <sub>2</sub> O8.0	R/Ra	3He/4He	Sample	MORB-type	Longitude, °W	Nb/Zr			
EW2D	N	90.821	62.9	0.049	—	—	0.124	7.75	EW2-1	N	90.821	0.019				
EW3C	E	90.983	47.2	0.157	2.45	0.869	—	—	EW7-4	E	91.275	0.086				
EW4D	T	91.060	58.3	0.115	2.51	0.788	0.248	7.80	EW10-1	E	91.364	0.111				
EW5C	E	91.076	51.1	0.159	2.52	0.864	—	—	EW11-1	E	91.404	0.108				
EW6D	T	91.183	54.7	0.112	2.25	0.853	—	7.97	EW15-1	T	91.607	0.091				
EW7D-a	E	91.275	50.9	0.173	2.57	0.838	0.307	7.98	EW16-2	E	91.746	0.087				
EW7D-b	T	91.275	54.5	0.136	2.61	0.831	—	—	EW17-1	E	91.803	0.098				
EW8C	E	91.357	39.1	0.240	2.61	0.824	—	—	EW17-4	E	91.803	0.099				
EW9D-a	T	91.322	51.8	0.128	2.53	0.834	0.279	8.07	EW19-1	E	91.957	0.098				
EW9D-b	T	91.322	57.0	0.123	2.57	0.775	—	—	EW20-1	E	92.012	0.099				
EW10D	E	91.364	38.4	0.239	2.53	0.833	0.354	—	EW25-1	E	92.320	0.105				
EW11D-a	E	91.404	30.9	0.440	2.43	—	0.149	7.30	EW28-1	E	92.519	0.096				
EW11D-b	E	91.404	33.5	0.333	2.59	—	—	—	EW29-1	T	92.618	0.073				
EW12D	E	91.486	36.2	0.237	2.56	0.835	0.359	7.31	EW32-2	T	92.880	0.068				
EW13D	E	91.560	39.0	0.271	2.48	0.833	—	—	EW33-1	T	92.971	0.075				
EW14C	E	91.608	33.0	0.223	2.25	0.848	—	—	EW38-2	T	93.268	0.068				
EW15D	T	91.607	58.0	0.161	2.20	0.803	0.305	7.37	EW41-1	T	93.093	0.074				
EW16D	E	91.746	53.1	0.200	2.95	0.741	0.480	7.71	EW41-7	T	93.093	0.071				
EW17D-a	E	91.803	57.6	0.264	3.23	0.688	0.555	7.77	EW45-2	T	93.352	0.063				
EW17D-b	E	91.803	59.4	0.255	3.21	0.664	—	—	EW48-4	T	93.657	0.075				
EW18D	E	91.881	57.2	0.198	2.51	0.819	—	—	EW49-1	T	93.871	0.073				
EW19D	E	91.957	38.6	0.240	2.77	0.817	0.432	7.55	EW50-1	T	93.777	0.082				
EW20D-a	E	92.012	60.2	0.225	2.61	0.709	—	—	EW56-2	T	94.240	0.057				
EW20D-b	E	92.012	58.4	0.231	2.72	0.737	0.423	8.05	EW58-2	T	94.350	0.061				
EW21D	E	92.051	50.8	0.212	2.83	0.821	—	—	EW62-1	T	94.662	0.056				
EW22D	E	92.157	51.5	0.254	2.90	0.853	—	—	EW63-1	N	94.747	0.038				
EW23D	E	92.222	50.4	0.194	2.56	0.854	—	7.54	EW63-2	T	94.747	0.052				
EW24D	E	92.244	53.6	0.193	2.43	0.826	—	—	EW67-1	T	95.033	0.060				
EW25D-a	E	92.320	55.7	0.233	2.45	0.821	0.324	7.71	EW69-1	T	95.213	0.061				
EW25D-b	E	92.320	56.9	0.226	2.47	0.804	—	—	EW70-1	T	95.317	0.051				
EW26C	E	92.373	54.5	0.402	2.45	0.816	—	—	EW71-1	N	95.602	0.030				
EW27D	E	92.427	46.4	0.151	2.27	0.857	—	—	EW73-1	T	95.702	0.047				
EW28D	E	92.519	53.7	0.189	2.31	0.865	0.261	7.45	EW77-2	N	96.191	0.029				
EW29D	T	92.618	50.8	0.135	2.20	0.840	0.233	7.38	EW79-1	N	96.725	0.035				
EW30D	E	92.695	43.5	0.149	2.30	0.867	—	—	EW80-2	N	96.630	0.018				
EW31D	T	92.822	47.8	0.135	2.32	0.832	—	7.39	EW83-5	N	96.818	0.026				

<sup>a</sup>For glass samples, station number, and type, (D)redge or Wax (C)ore shown. Samples from same station with significantly similar major element data were grouped together. H<sub>2</sub>O and <sup>3</sup>He/<sup>4</sup>He data were determined from one sample representative of the group. All samples from R/V *Maurice Ewing* cruise EW00-04 except samples 1538–1557 which are a reanalysis of *Avin* samples collected from 95W propagating rift area by *Hey et al.* [1992] and dredges A6 and A13.

PR, propagating rift; DR, dying rift; NG, North Graben. MORB type based on K/Ti ratio: N, N-MORB; T, T-MORB; E, E-MORB. Mg#, atomic (Mg/Mg+Fe). Na8.0, Ca8.0/A18.0, and H<sub>2</sub>O8.0 are derived from oxide values of Na<sub>2</sub>O, CaO, Al<sub>2</sub>O<sub>3</sub> and H<sub>2</sub>O corrected to 8.0 wt. % MgO. He R/Ra, (<sup>3</sup>He/<sup>4</sup>He)/atmospheric ratio. Gas trapped in vesicles was released by in vacuo crushing, and the separated helium was analyzed by mass spectrometry. Nb/Zr determined on whole rock samples; MORB type based on K/Ti ratios of the corresponding glass samples.



### 3. Results

#### 3.1. Swell Topography and Crustal Thickness

[6] The Galápagos hot spot swell is apparent in the gradual shoaling of sea floor depths along the western GSC over a distance of  $\sim 800$  km (Figure 1). Ridge axis depths along the western GSC decrease from  $\sim 3500$  m at  $97.7^\circ\text{W}$  to  $<1700$  m at  $91.4^\circ\text{W}$  (Figure 2a). Part of this  $\sim 1800$  m change in axial depth is a result of a systematic change in axial morphology. Far from the Galápagos hot spot (west of  $95^\circ\text{W}$ ), the GSC is associated with a 20–40 km wide, 400–1000 m deep rift valley resembling that of the slow-spreading Mid-Atlantic Ridge. Within  $\sim 300$  km of the Galápagos hot spot (east of  $\sim 92.7^\circ\text{W}$ ) the GSC is associated with a 400–700 m axial high typical of the fast-spreading East Pacific Rise. These differences in axial topography can account for a significant amount of the depth variation observed along the western Galápagos swell. *Canales et al.* [2002] found that a low-pass filter with a cutoff wavelength of 85 km effectively removes the short-wavelength contribution of variations in axial topography while preserving the longer wavelength anomaly associated with the hot spot swell. They found that  $\sim 60\%$  of the observed variation in axial depth along the western Galápagos swell is related to changes in axial morphology. After correcting for these effects, the maximum swell amplitude near  $91^\circ\text{W}$  is estimated to be  $\sim 700$  m (Figure 2a). Coinciding with this topographic swell is a regional mantle Bouguer anomaly (MBA) that becomes increasingly negative along the GSC toward the hot spot, with a minimum of  $-70$  mGal at  $\sim 91.25^\circ\text{W}$  (Figure 2b).

[7] Crustal thickness variations along the western Galápagos swell are constrained by three ridge-parallel, wide-angle seismic refraction profiles at  $97^\circ\text{W}$ ,  $94.25^\circ\text{W}$ , and  $92^\circ\text{W}$ , and by two-way Moho reflection times observed on multichannel seismic reflection profiles collected on ridge-parallel, off-axis profiles between  $91.5^\circ\text{W}$  and  $95.5^\circ\text{W}$  (Figure 1). Crustal thickness along the western GSC increases from  $5.6 \pm 0.2$  km at  $97^\circ\text{W}$  to

$\sim 7.9$  km at  $91.5^\circ\text{W}$ , an increase of  $\sim 2.3$  km (Figure 2c). The significant thickening of the crust east of  $94^\circ\text{W}$  indicates that the primary effect of the hot spot on melt productivity beneath the GSC is confined to a distance less than  $\sim 400$  km from the center of the hot spot.

[8] The effects of crustal thickening on the along-axis swell and gravity anomalies can be calculated assuming that the smoothed crustal thickness profile (best fitting polynomial function shown as black curve in Figure 2c) is compensated by local Airy isostasy. Assuming average water, crust, and mantle densities of  $1000$  kg/m<sup>3</sup>,  $2770$  kg/m<sup>3</sup>, and  $3300$  kg/m<sup>3</sup>, respectively, *Canales et al.* [2002] showed that, on average, crustal thickness variations support  $\sim 50\%$  of the swell depth anomaly east of  $94^\circ\text{W}$ . After computing the gravitational effects of the crust, *Canales et al.* [2002] also found that the crust accounts for an average of  $\sim 60\%$  of the observed MBA east of  $94^\circ\text{W}$ . That portion of the swell topography not explained by crustal thickness variation is called the residual mantle swell anomaly, or RMSA, and is shown in Figure 3b for the most plume influenced part of the ridge east of  $94^\circ\text{W}$ . The remaining gravity anomaly is the residual MBA, or RMBA. The RMBA becomes increasingly negative toward the east reaching a minimum of  $\sim -25$  mGal at  $92.25^\circ\text{W}$ , where it coincides with the largest ( $\sim 300$  m) RMSA (Figure 3b). Both of these anomalies occur near the intersection of the GSC and the Wolf-Darwin seamount chain, rather than farther to the east where the ridge crest is closer to the hot spot. A secondary minimum in RMBA and peak in RMSA occurs near  $91.3^\circ\text{W}$  where another small seamount chain intersects the GSC (Figure 3b); however, these anomalies are less well constrained because of a lack of seismic control on crustal thickness east of  $91.5^\circ\text{W}$  (Figure 2c).

[9] The negative RMBA indicates that anomalously low mantle densities are present beneath the GSC with the lowest densities near the hot spot. The ratio of the variation in RMBA and RMSA is well explained by calculations that assume the excess swell topography is isostatically compensated by mantle density variations confined to

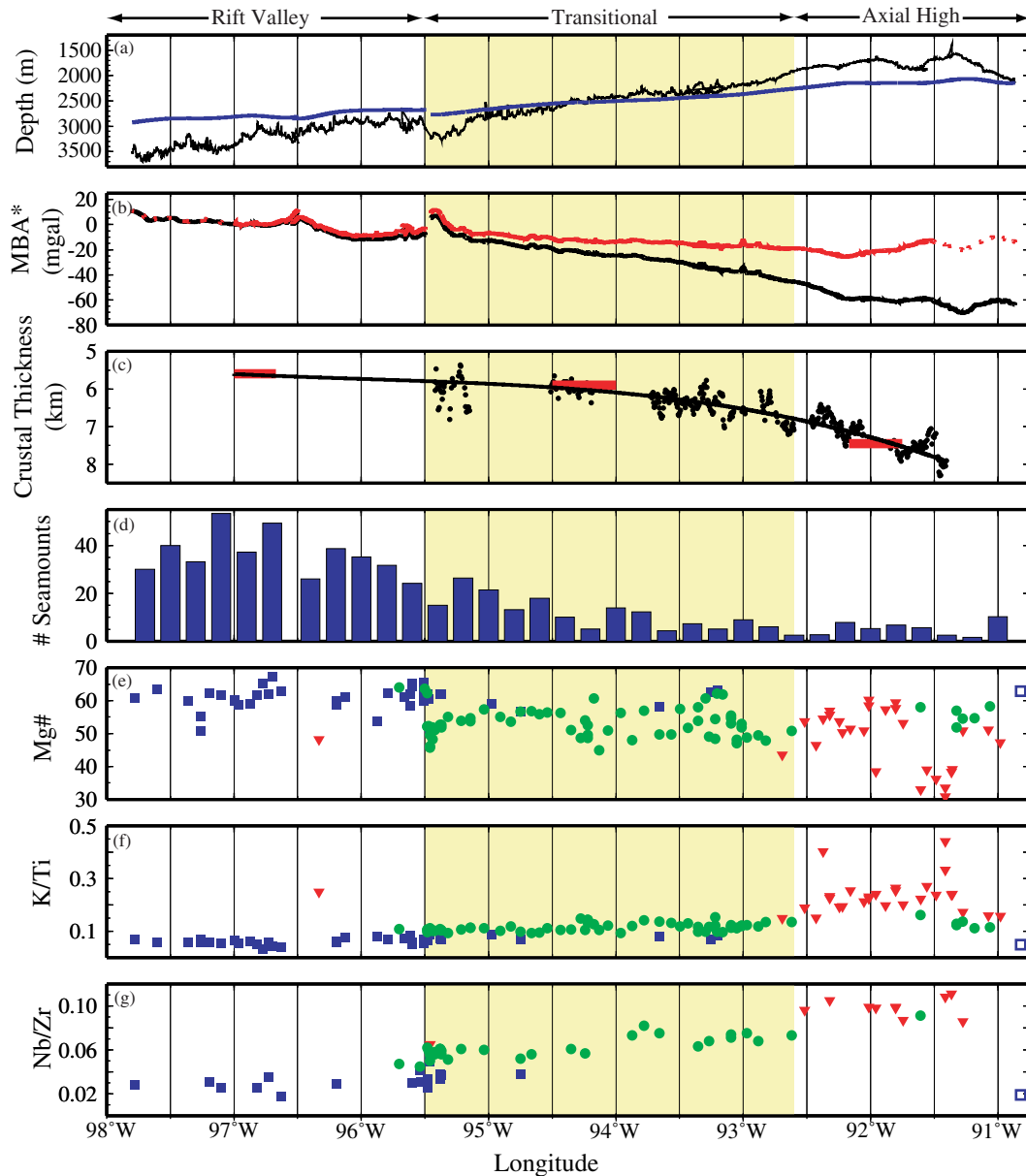


**Figure 2.** Geophysical, volcanological, and geochemical variations along the western GSC showing the following: (a) depth of ridge axis (black line) and Galápagos swell (blue line); swell depth is corrected for variations in axial topography along western GSC. (b) Mantle Bouguer anomaly (black line) and residual mantle Bouguer anomaly (RMBA, red line; red dots where unconstrained by crustal thickness measurements). (c) Crustal thickness along GSC from *Canales et al.* [2002] including estimates from ocean bottom seismic refraction experiments (red horizontal bars) and two-way Moho reflection travel times converted to crustal thickness (dots); black line is best fitting polynomial function to crustal thickness data. (d) Abundance of small seamounts in axial zone of GSC determined from high-resolution multibeam bathymetry data; seamount abundance calculated in ten minute longitude bins. (e) Mg # ( $100[\text{atomic MgO}/(\text{MgO}+\text{FeO})]$ ) for lava samples from GSC. (f) K/Ti. (g) Nb/Zr. In Figures 2e–2g, blue squares denote normal mid-ocean ridge basalts (N-MORB), inverted red triangles enriched MORB (E-MORB), and green circles transitional MORB (T-MORB). Solid symbols are samples from the GSC; open symbols are from the 91°W fracture zone. The domains of axial morphology (rift valley, transitional, axial high) along the GSC are shown for reference.

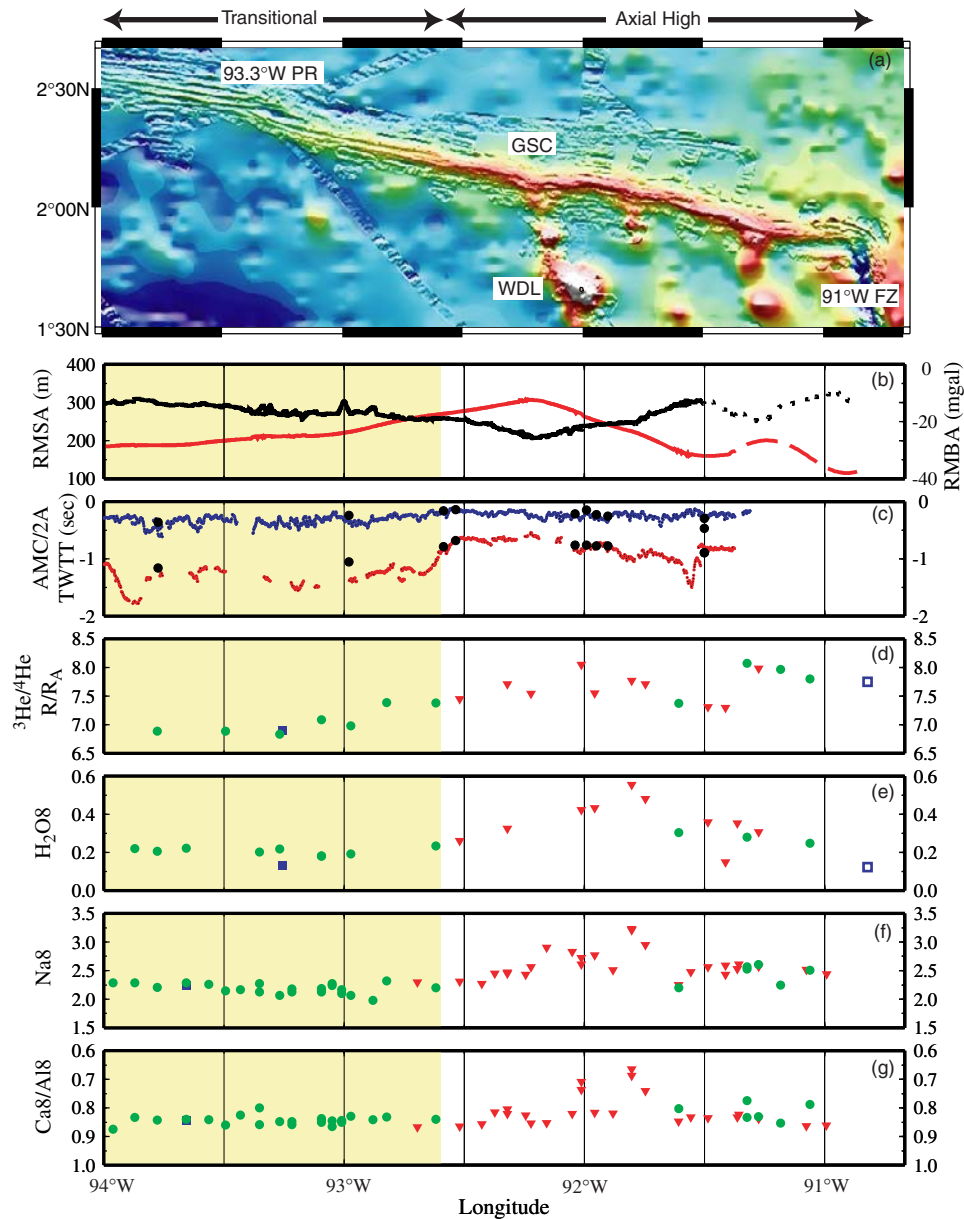


**Figure 3.** Correlated variations in morphology, axial structure, and lava chemistry along the most plume-influenced portion of the western GSC east of 94°W, showing the following: (a) bathymetry (purple-blue, deep; yellow-red, shallow) from *Canales et al.* [1997] and *Smith and Sandwell* [1997], and this study; location of fracture zone (FZ) at 91°W and propagating rift (PR) at 93.3°W shown for reference. (b) Red line (dashed where unconstrained by crustal thickness) shows residual mantle swell anomaly (RMSA), that portion of the swell topography not predicted by crustal thickness variation; RMBA (black line and dots), from Figure 2b, shown for comparison. (c) Two-way travel time to base of seismic layer 2A (blue) and top of axial magma chamber (red) from multichannel seismic reflection data (black dots show picks from cross-axis profiles, all other picks are from along-axis profiles). (d)  $^3\text{He}/^4\text{He}$  R/R<sub>A</sub>, (e) H<sub>2</sub>O<sub>8</sub>, (f) Na<sub>8</sub>, and (g) Ca<sub>8</sub>/Al<sub>8</sub> (note reversed scale), for GSC lavas. Symbols in Figures 3d–3g are same as in Figure 2. Note that west of 92.7°W the axial high disappears and a distinct transitional morphology lacking either an axial high or axial valley is present. This change in axial morphology correlates with significant changes in axial structure (Figure 3c) and lava chemistry (Figures 3d–3g). The largest residual swell anomaly (Figure 3b), shallowest axial magma chamber (Figure 3c), and peaks in  $^3\text{He}/^4\text{He}$ , H<sub>2</sub>O, and Na<sub>8</sub> (Figures 3d–3f) all occur between 91.8°W and 92.25°W near where the Wolf-Darwin lineament and a second similar seamount chain intersect the GSC. A secondary peak in both residual swell anomaly and  $^3\text{He}/^4\text{He}$  occurs near 91.3°W where a third seamount chain intersects the GSC.



depths of 50–100 km [Canales *et al.*, 2002]. We see no need to invoke additional dynamic topography, unrelated to mantle density variations, such as those that may be caused by regional asthenospheric pressure gradients [e.g., Phipps Morgan *et al.*, 1995; Yale and Phipps Morgan, 1998]. The simplest case of passive mantle upwelling and adiabatic decompression melting requires only a small increase in mantle potential temperature of  $\sim 30^\circ\text{C}$  to thicken the crust by  $\sim 2.3$  km, as observed along the western GSC between  $98^\circ\text{W}$  and  $91^\circ\text{W}$ . The density reduction associated with this increase in mantle temperature, as well as the increased mantle depletion [Oxburgh and Parmentier, 1977] due to melting, can account for part, but not all, of the mantle density variation required to explain the RMBA and excess swell topography. This excess buoyancy may be caused by melt in the mantle and/or depletion due to melting of the upwelling plume far from the ridge axis and the subsequent transport of this depleted residuum northward toward the GSC.

### 3.2. Depth of Axial Magma Lens, Thickness of Seismic Layer 2A, and Axial Morphology

[10] At an intermediate spreading-rate ridge like the GSC, lithospheric thermal structure and its effect on axial morphology are expected to be particularly sensitive to small changes in magma supply. The along-axis variation in crustal thickness (Figure 2c) reveals a systematic change in magma supply, while the depth at which magma resides in the crust at the ridge axis (Figure 3c) constrains thermal gradients in the axial lithosphere. West of  $\sim 95^\circ\text{W}$ , where a rift valley characterizes the axial morphology, we find the thinnest crust along the western GSC (5.6–6 km). Between  $95^\circ\text{W}$  and  $92.7^\circ\text{W}$ , where axial morphology is transitional, displaying neither an axial valley nor a topographic high, crustal thickness is 6–7 km and the top of an axial magma chamber (AMC) is at depths of 2.5–4.25 km (1.0–1.7 two-way travel time (TWTT)). East of  $92.7^\circ\text{W}$ , where the GSC is associated with an axial high, the AMC is significantly shallower (0.55–0.9 s TWTT or  $\sim 1.38$ –2.25 km depth), and the crust is 7–8 km

thick. Although the variation in magma supply along the GSC is very gradual, the transition from one type of topographic regime to another is fairly abrupt. For example, the appearance of the axial high near  $92.7^\circ\text{W}$  occurs over an along-axis distance of only  $\sim 20$  km (Figure 3a). The development of the axial high correlates remarkably well with a rapid shoaling of the AMC by  $>1$  km and an approximate halving of the thickness of seismic layer 2A from 0.3–0.5 s TWTT ( $\sim 300$ –500 m) to 0.15–0.35 s TWTT ( $\sim 150$ –350 m), over the same along-axis distance. The correlation between AMC depth and axial topography supports the notion that axial topography is directly linked to the thermal structure and thus the strength of the axial lithosphere [Chen and Morgan, 1990]. The abrupt changes in both AMC depth and axial morphology, despite only modest changes in crustal thickness, support the hypothesis of Phipps Morgan and Chen [1993] of a threshold effect in which small changes in magma supply lead to significant changes in axial thermal structure, magma chamber depth, and axial morphology.

### 3.3. Seamount Abundance and Magma Supply-Related Variations in Eruptive Style

[11] The number of small seamounts or volcanic edifices present in the axial zone of the GSC has been determined using high-resolution multibeam bathymetric data and a numerical algorithm that identifies closed, concentric contours that meet certain shape and height criteria (Figure 2d). Seamount densities have been calculated using a maximum likelihood model [Smith and Cann, 1992]. The number of seamounts in the axial zone decreases significantly as the Galápagos hot spot is approached, suggesting a change from dominantly point-source to fissure-fed volcanism as magma supply increases. West of  $95.5^\circ\text{W}$ , where magma supply is lower, the number of seamounts per unit area ( $\sim 279 \pm 16$  per  $10^3$  km<sup>2</sup>) is similar to values observed at the slow-spreading Mid-Atlantic Ridge [Smith and Cann, 1992; Magde and Smith, 1995]. In contrast, east of  $92.7^\circ\text{W}$ , where magma supply is higher, seamount density ( $50 \pm 9$  per  $10^3$  km<sup>2</sup>) is similar to observations at the fast-spreading East Pacific Rise [Abers *et al.*, 1988].



Thus the western GSC displays the same range in seamount density observed along the global mid-ocean ridge system suggesting that both spreading rate and magma supply are important factors controlling the style of constructional volcanism (point source versus fissure fed eruptions) at oceanic spreading centers.

### 3.4. Geochemical Constraints on Source Composition and Mantle Melting

[12] As the Galápagos hot spot is approached from the west along the GSC there are systematic variations in basalt chemistry, first described by *Schilling et al.* [1982], that correlate with the geophysical variations described above (Figures 2 and 3). Although sample spacing in this study (<10 km) is much closer than the 40–50 km by *Schilling et al.* [1982], and our samples are more precisely located on the ridge axis using multibeam bathymetry, we find a similar long-wavelength pattern of geochemical variation as reported by Schilling and colleagues. For example, average lava Mg # (atomic MgO/(MgO+FeO)) decreases progressively from west to east with the lowest Mg # (most fractionated) lavas erupting along the most plume influenced portion of the ridge (Figure 2e). This indicates an eastward increase in the degree of crystallization that correlates with the presence and shoaling of the AMC. Incompatible elements such as K<sub>2</sub>O, TiO<sub>2</sub>, and H<sub>2</sub>O all increase along the western GSC toward the 91°W fracture zone, indicating the presence of a plume source enriched in volatiles and other incompatible elements as described by *Schilling et al.* [1982].

[13] Variations in ratios of incompatible elements including K/Ti and Nb/Zr, and isotopes such as <sup>3</sup>He/<sup>4</sup>He, largely reflect differences in the mantle source undergoing melting. These ratios therefore provide information on the relative proportion of plume-derived versus ambient mantle in GSC magmas. In this paper, basalts with a K/Ti ratio <0.09 have been designated as N-MORB; T-MORB have 0.09 < K/Ti <0.15, and E-MORB have K/Ti >0.15. The propagating rift tip at 95.5°W appears to define the western limit of plume-affected mantle on the basis of variations in K/Ti (Figure 2f) and Nb/Zr (Figure 2g). West

of 95.5°W, within the rift valley domain, chemically normal mid-ocean ridge basalt, or N-MORB, with K/Ti <0.09 is the dominant rock type recovered. In this distal region, which is unaffected by the Galápagos plume, Nb/Zr is <0.04 and <sup>3</sup>He/<sup>4</sup>He is close to 7 times atmospheric values (*R<sub>A</sub>*). Between 95.5°W and 92.7°W, K/Ti values of 0.09–0.15 define compositions that are transitional between N-MORB and incompatible-element enriched basalts or E-MORB. These transitional basalts (or T-MORB) have Nb/Zr and <sup>3</sup>He/<sup>4</sup>He (Figure 3d) ratios that generally increase eastward reaching values of ~0.08 and ~7.4 *R<sub>A</sub>*, respectively, near 92.7°W. East of 92.7°W, E-MORB is dominant, with K/Ti ratios >0.15, Nb/Zr > 0.09, and <sup>3</sup>He/<sup>4</sup>He >7.5 *R<sub>A</sub>*. Although the Galápagos Islands represent a “high <sup>3</sup>He/<sup>4</sup>He” hot spot, having <sup>3</sup>He/<sup>4</sup>He ratios up to 30 times the atmospheric values in the western and southern parts of the archipelago [*Graham et al.*, 1993; *Kurz and Geist*, 1999], the highest <sup>3</sup>He/<sup>4</sup>He ratios observed along the western GSC are only 8.0–8.1 *R<sub>A</sub>*, similar to basalts from many ridges with no plume influence [*Graham*, 2002].

[14] Basalt concentrations of incompatible elements such as H<sub>2</sub>O, Na, Ca, and Al may in part reflect source composition, but these elements are also strongly influenced by the partial melting process [*Jacques and Green*, 1980; *Langmuir et al.*, 1992]. East of ~92.7°W, incompatible elements H<sub>2</sub>O<sub>8</sub> (Figure 3e) and Na<sub>8</sub> (Figure 3f) (H<sub>2</sub>O and Na<sub>2</sub>O corrected for magmatic differentiation to 8 wt% MgO, respectively) show maximum values, and Ca<sub>8</sub>/Al<sub>8</sub> ratios (Figure 3g) are minimum. This is consistent with the results of *Schilling et al.* [1982] and *Fisk et al.* [1982] who also report high Na<sub>2</sub>O, low CaO/Al<sub>2</sub>O<sub>3</sub>, and high H<sub>2</sub>O along the GSC near 91°–92°W. Although some of these chemical variations can be accounted for by increasing incompatible element enrichment in the mantle source east of 92.7°W, variations in Na<sub>8</sub>, and especially Ca<sub>8</sub>/Al<sub>8</sub>, are more likely to be controlled by variations in the extent of melting than by source compensation. Thus, paradoxically, the region east of 92.7°W with the thickest crust and the strongest plume source contribution has major element compositions (e.g., high Na<sub>2</sub>O and



low CaO/Al<sub>2</sub>O<sub>3</sub>) that suggest mean extents of partial melting that are relatively low.

#### 4. Discussion

[15] The regional geophysical, geochemical, and volcanological correlations observed along the western GSC clearly reflect the combined effects of changes in mantle source composition and melt generation processes on the thickness, composition, and structure of oceanic crust. The maximum values in K/Ti (>0.4), Nb/Zr (>0.10), H<sub>2</sub>O<sub>8</sub> (>0.5 wt%), <sup>3</sup>He/<sup>4</sup>He (8.1 R<sub>A</sub>), Na<sub>8</sub> (~3.2), crustal thickness (7.9 km), and residual swell anomaly (~300 m), and minima in axial depth (<1700 m), Ca<sub>8</sub>/Al<sub>8</sub> (<0.7), Mg # (<40), magma chamber depth (<1.5 km) and residual gravity anomaly (−25 mGal) all occur between 91.3°W and 92.25°W indicating a maximum plume influence in this region. The increased melt production beneath the most plume-influenced part of the GSC results in a hotter, weaker axial lithosphere leading to formation of an axial-high morphology, the stabilization of axial magma chambers at increasingly shallow crustal depths, and the dominance of fissure-fed over point-source volcanism.

[16] The increased melt production along the most plume-influenced part of the GSC can be related to melting from a larger region of a hydrous, and otherwise incompatible element-enriched mantle, with slightly elevated temperature (Figure 4). The recognition of the importance of water in expanding the zone of partial melting, leading to enhanced melt production was first noted in the Galápagos region by Schilling *et al.* [1982] and Fisk *et al.* [1982] and also in the region around the Azores hot spot [Schilling *et al.*, 1980; Bonatti, 1990]. By depressing the solidus [Kushiro, 1968], the presence of excess water increases the depth at which melting begins and expands the volume of mantle undergoing melting [Schilling *et al.*, 1980; Plank and Langmuir, 1992]. We reconcile the association of increased melt production with lower mean extents of melting along the most plume-influenced part of the GSC by noting that the extent of melting within the expanded zone is likely to be low [Braun *et al.*, 2000]. Thus the total melt volume close to the

hot spot has, in addition to the contribution from normal anhydrous melting, a contribution from a large volume undergoing low extents of partial melting. Although the total melt production is increased, the mean extent of melting for the total melt volume is reduced. The decrease in the proportion of plume-affected mantle westward along the GSC results in a progressive decrease in the amount of low-degree melts derived from the hydrous melting region and thus a decrease in crustal thickness and incompatible element enrichment (Figure 4b).

[17] The low <sup>3</sup>He/<sup>4</sup>He ratio of GSC lavas suggests that even the most plume-affected mantle beneath the GSC has been degassed of its most volatile components. One explanation of these low <sup>3</sup>He/<sup>4</sup>He ratios that has been suggested for other plume-ridge systems [Poreda *et al.*, 1993; Graham *et al.*, 1999] is a small amount of melting in the upwelling plume. If this slightly depleted plume mantle is subsequently transported to the ridge axis and undergoes additional decompression melting associated with plate spreading, it will acquire an anomalous chemical buoyancy that could explain the excess swell topography observed along the western GSC (Figure 3b). However, this explanation requires a mechanism that decouples He from K, H<sub>2</sub>O and other incompatible elements enriched in GSC basalts during plume upwelling, melting, and lateral transport to the ridge. Alternatively, the plume material that is present beneath the GSC may have an inherently low <sup>3</sup>He/<sup>4</sup>He ratio. White *et al.* [1993] concluded that the Galápagos plume is heterogeneous and chemically zoned with distinctive northern, central, and southern components. Graham *et al.* [1993] and Kurz and Geist [1999] reported relatively low <sup>3</sup>He/<sup>4</sup>He ratios for the Wolf-Darwin and Pinta lavas, respectively, in contrast to Fernandina which has a high <sup>3</sup>He/<sup>4</sup>He ratio. In this case the low <sup>3</sup>He/<sup>4</sup>He ratios observed at the GSC reflect sampling of the low <sup>3</sup>He/<sup>4</sup>He component of the plume source and the excess mantle buoyancy observed beneath the western GSC must arise from another mechanism, such as melt retention in the mantle. Additional geochemical and geophysical data

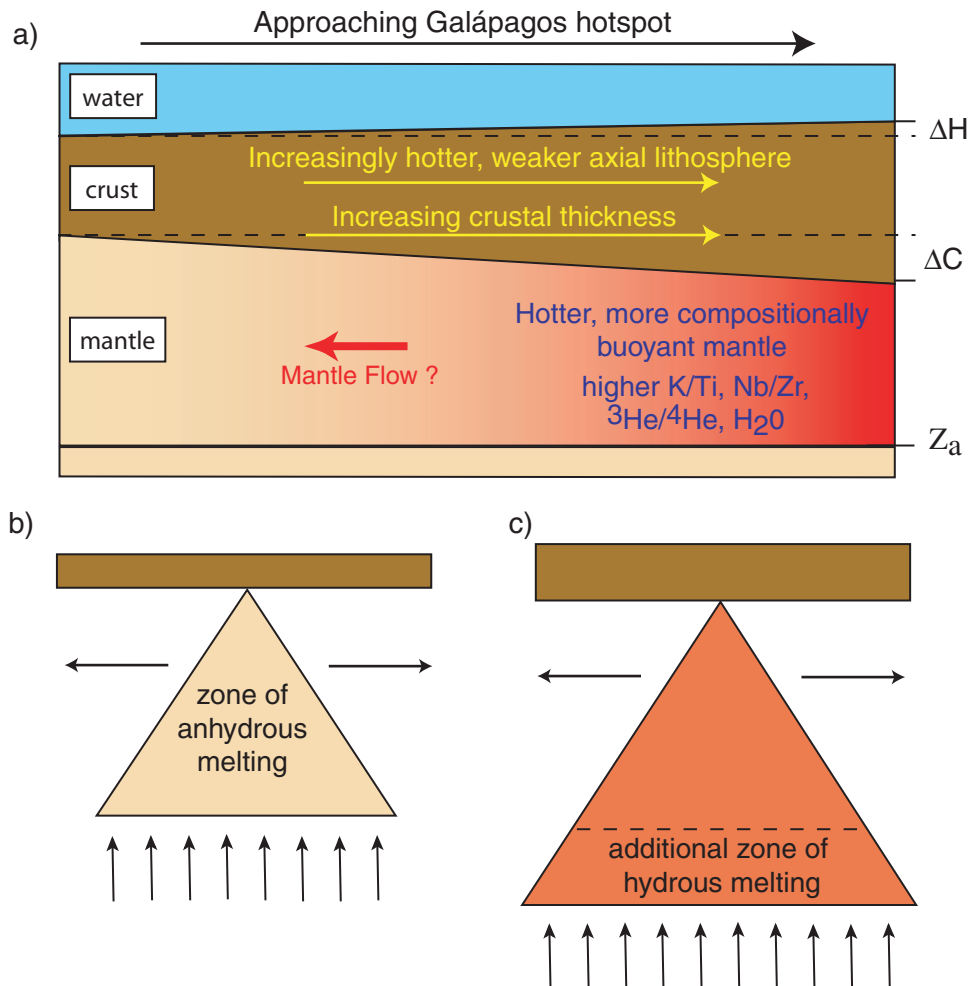


**Figure 4.** The geophysical, geochemical, and volcanological correlations observed along the western GSC can be explained by the combined effects of changes in mantle source composition and melt generation processes on the thickness, composition, and structure of oceanic crust as Galápagos plume mantle feeds the GSC, and spreads laterally along the ridge axis. With available geophysical and geochemical constraints, we do not know if the GSC is sampling a broad, radially spreading plume head or whether there is channelized flow of plume material to and along the GSC. (a) Isostatic support for the Galápagos swell ( $\Delta H = 0.7\text{ km}$ ) comes from variations in crustal thickness ( $\Delta C = 2.3\text{ km}$ ) along the GSC, thermal buoyancy associated with along-axis mantle potential temperature variations ( $\Delta T = 30^\circ\text{C}$ ), and a compositionally buoyant mantle distributed to mantle depths of 50–100 km ( $Z_a$ ). The increased melt production beneath the plume-influenced part of the GSC results in a hotter, weaker axial lithosphere leading to formation of an axial high morphology, the stabilization of axial magma chambers at increasingly shallow crustal depths, and the dominance of fissure-fed over point-source volcanism. Cross-sections for “normal” (distal) and plume-influenced (proximal) portions of the GSC are shown in Figures 3b and 3c, respectively. Melting from a larger region of a hydrous, and otherwise incompatible-element-enriched mantle, with slightly elevated temperatures can explain both the thicker crust, and the increase in K/Ti,  $\text{Na}_2\text{O}$ , Nb/Zr,  $^3\text{He}/^4\text{He}$ , and  $\text{H}_2\text{O}$  content of lavas along the most plume-influenced part of the GSC. See text for discussion.

from the Galápagos region are required to distinguish between these two alternatives.

[18] The largest residual swell anomaly (Figure 3b), the shallowest axial magma chamber (Figure 3c), the highest values of  $^3\text{He}/^4\text{He}$ ,  $\text{H}_2\text{O}$ , and Na8

(Figures 3d–3f), and the lowest values of Ca8/Al8 (Figure 3g) all occur between  $91.8^\circ\text{W}$  and  $92.25^\circ\text{W}$  near where the Wolf-Darwin lineament and a second similar seamount chain intersect the GSC (Figure 3a). A secondary peak in both residual swell anomaly and  $^3\text{He}/^4\text{He}$  occurs near  $91.3^\circ\text{W}$



where a third seamount chain intersects the GSC. The anomalies near 92°W coincide with the approximate location of a maximum in  $^{87}\text{Sr}/^{86}\text{Sr}$  and a minimum in  $^{143}\text{Nd}/^{144}\text{Nd}$  previously reported by *Verma and Schilling* [1982] and *Verma et al.* [1983]. These geophysical and geochemical anomalies indicate a strong thermal and chemical plume influence in this area, supporting the *Morgan* [1978] hypothesis of channeling of plume material to the GSC along the Wolf-Darwin lineament. However, the association of bathymetric, geochemical, and geophysical anomalies with the intersection of two other small seamount chains with the GSC (e.g., the peaks in  $\text{H}_2\text{O}$  and Na8 near 91.8°W, and in  $^3\text{He}/^4\text{He}$ , K/Ti, Nb/Zr and residual swell depth at 91.3°W) may indicate a more complicated pattern of plume-ridge interaction with channelized flow of plume material to the ridge in at least three different locations between 91.3°W and 92.25°W. Alternatively, these seamount chains may be lithospheric cracks that are sampling a broad, radially spreading plume head that is being entrained by upwelling beneath the GSC. Additional isotope analyses of basalts from the GSC and these seamount chains and improved geophysical constraints on mantle properties beneath the GSC and its southern ridge flank will be required to more fully understand how the Galápagos plume and ridge are interacting.

## 5. Conclusions

[19] The correlated variations in geophysical, geochemical, and volcanological manifestations of plume-ridge interaction observed along the western Galápagos Spreading Center can be explained by the combined effects of changes in mantle temperature and source composition on melt generation processes, and the consequences of these variations on magma supply, axial thermal structure, basalt chemistry, and styles of volcanism. Key elements of this interpretation include (1) isostatic support for the Galápagos swell by a combination of crustal thickening (2.3 km between 98°W and 90.5°W), thermal buoyancy associated with a comparatively small along-axis variation in mantle potential temperature ( $\sim 30^\circ\text{C}$ ), and a compositionally buoyant, melt-depleted mantle; (2) melting from a larger

region of a hydrous, and otherwise incompatible-element-enriched mantle, with slightly elevated temperatures, to explain both the thicker crust, and the increase in K/Ti,  $\text{Na}_2\text{O}$ , Nb/Zr,  $^3\text{He}/^4\text{He}$ , and  $\text{H}_2\text{O}$  content of lavas along the most plume-influenced part of the GSC; and (3) the association of increased melt production with a hotter, weaker axial lithosphere leading to formation of an axial high morphology, the stabilization of axial magma chambers at increasingly shallow crustal depths, and the dominance of fissure-fed over point-source volcanism. Our results document a clear link between magma supply and variations in axial morphology, AMC depth and volcanic style that are largely independent of spreading rate. Along the western GSC even small changes in magma supply result in changes in axial thermal structure that have pronounced effects on axial morphology and crustal accretion processes.

## Acknowledgments

[20] We thank the officers, crew and scientific complement on R/V *Maurice Ewing* leg EW00-04 for their professionalism, expert help, and hard work collecting the data presented in this report. We also thank John Lupton for access to his helium isotope lab, which is supported by the NOAA Vents Program. We are very grateful to the Ecuadorian government and the Parque Nacional Galápagos for permission to work in their waters. We thank Bill White, Jean-Guy Schilling, and Doug Toomey for reviews of a previous version of this manuscript, and Charlie Langmuir for discussions concerning the relationships among hydrous melting, total melt production and mean extents of melting. This research was supported by NSF OCE-9819117 to Woods Hole Oceanographic Institution, NSF OCE-9818632 to University of Hawaii, and NSF OCE-9818886 to Oregon State University. This is Woods Hole Oceanographic Institution Contribution number 10715 and SOEST contribution 5994.

## References

- Abers, G. A., B. Parsons, and J. K. Weissel, Seamount abundances and distributions in the Southeast Pacific, *Earth Planet. Sci. Lett.*, **87**, 137–151, 1988.
- Braun, M. G., G. Hirth, and E. M. Parmentier, The effects of deep damp melting on mantle flow and melt generation beneath mid-ocean ridges, *Earth Planet. Sci. Lett.*, **176**, 339–356, 2000.
- Bonatti, E., Not so hot “hot spots” in the oceanic mantle, *Science*, **250**, 107–111, 1990.
- Canales, J. P., J. J. Danobeitia, R. S. Detrick, E. E. E. Hooft, R. Bartolomé, and D. Naar, Variations in axial morphology



- along the Galápagos Spreading Center and the influence of the Galápagos hot spot, *J. Geophys. Res.*, *102*, 27,341–27,354, 1997.
- Canales, J. P., G. Ito, R. S. Detrick, and J. Sinton, Compensation mechanism of the Galápagos Swell, *Earth Planet. Sci. Lett.*, in press, 2002.
- Chen, Y., and W. J. Morgan, Rift valley/no rift valley transition at mid-ocean ridges, *J. Geophys. Res.*, *95*, 17,571–17,581, 1990.
- Christie, D. M., and J. M. Sinton, Evolution of abyssal lavas along propagating segments of the Galápagos Spreading Center, *Earth Planet. Sci. Lett.*, *56*, 321–335, 1981.
- Christie, D. M., and J. M. Sinton, Major element constraints on melting, differentiation and mixing of magmas from the Galápagos 95.5°W propagating rift system, *Contrib. Mineral. Petrol.*, *94*, 274–288, 1986.
- DeMets, C., R. G. Gordon, D. F. Argus, and S. Stein, Current plate motions, *Geophys. J. Int.*, *101*, 425–478, 1990.
- Fisk, M. R., A. E. Bence, and J.-G. Schilling, Major element chemistry of Galápagos Rift zone magmas and their phenocrysts, *Earth Planet. Sci. Lett.*, *61*, 171–189, 1982.
- Graham, D. W., Noble gas isotope geochemistry of mid-ocean ridge and ocean island basalts; characterization of mantle source reservoirs, in *Noble Gases in Geochemistry and Cosmochemistry*, edited by D. Porcelli, R. Wieler, and C. Ballentine, Mineral. Soc. Am., Washington, D.C., in press, 2002.
- Graham, D. W., D. M. Christie, K. S. Harpp, and J. E. Lupton, Mantle plume helium in submarine basalts from the Galápagos Platform, *Science*, *262*, 2023–2026, 1993.
- Graham, D. W., K. T. M. Johnson, L. M. Douglas Priebe, and J. E. Lupton, Hot spot-ridge interaction along the Southeast Indian Ridge near Amsterdam and St. Paul Islands: Helium isotope evidence, *Earth Planet. Sci. Lett.*, *167*, 297–310, 1999.
- Hey, R. N., Tectonic evolution of the Cocos-Nazca spreading center, *Geol. Soc. Am. Bull.*, *88*, 1404–1420, 1977.
- Hey, R. N., J. M. Sinton, M. C. Kleinrock, R. N. Yonover, K. C. Macdonald, S. P. Miller, R. C. Searle, D. M. Christie, T. M. Atwater, N. H. Sleep, H. P. Johnson, and C. A. Neal, ALVIN investigation of an active propagating rift system, Galápagos 95.5°W, *Mar. Geophys. Res.*, *14*, 207–226, 1992.
- Ito, G., and J. Lin, Oceanic spreading center-hot spot interactions: Constraints on along-isochron bathymetric and gravity anomalies, *Geology*, *7*, 657–660, 1995a.
- Ito, G., and J. Lin, Mantle temperature anomalies along the present and paleoaxes of the Galápagos Spreading Center as inferred from gravity analyses, *J. Geophys. Res.*, *100*, 3733–3745, 1995b.
- Jacques, A. L., and D. H. Green, Anhydrous melting of peridotite at 0–15 kb pressure and genesis of tholeiitic basalts, *Contrib. Mineral. Petrol.*, *73*, 287–310, 1980.
- Kurz, M. D., and D. Geist, Dynamics of the Galápagos hot spot from helium isotope geochemistry, *Geochim. Cosmochim. Acta*, *63*, 4139–4156, 1999.
- Kushiro, I., The system forsterite-diopside-silica with and without water at high pressures, *Am. J. Sci.*, *267A*, 269–294, 1968.
- Langmuir, C. H., E. M. Klein, and T. Plank, Petrological systematics of mid-ocean ridge basalts: Constraints on melt generation beneath ocean ridges, in *Mantle Flow and Melt Generation at Mid-Ocean Ridges*, *Geophys. Monogr. Ser.*, vol. 71, edited by J. Phipps Morgan et al., pp. 183–280, AGU, Washington, D.C., 1992.
- Magde, L. S., and D. K. Smith, Seamount volcanism at the Reykjanes Ridge: Relationship to the Iceland hot spot, *J. Geophys. Res.*, *100*, 8449–8468, 1995.
- Morgan, W. J., Rodriguez, Darwin, Amsterdam . . . A second type of hot spot island, *J. Geophys. Res.*, *83*, 5355–5360, 1978.
- Oxburgh, E. R., and E. M. Parmentier, Compositional and density stratification in oceanic lithosphere – causes and consequences, *Geol. Soc. London*, *133*, 343–355, 1977.
- Phipps Morgan, J., and Y. J. Chen, The genesis of oceanic crust: Magma injection, hydrothermal circulation, and crustal flow, *J. Geophys. Res.*, *98*, 6283–6297, 1993.
- Phipps Morgan, J., W. J. Morgan, Y.-S. Zhang, and W. H. F. Smith, Observational hints for a plume-fed, suboceanic asthenosphere and its role in mantle convection, *J. Geophys. Res.*, *100*, 12,753–12,767, 1995.
- Plank, T., and C. H. Langmuir, Effects of the melting regime on the composition of the oceanic crust, *J. Geophys. Res.*, *97*, 19,749–19,770, 1992.
- Poreda, R. J., J.-G. Schilling, and H. Craig, Helium isotope ratios in Easter Microplate basalts, *Earth Planet. Sci. Lett.*, *119*, 319–329, 1993.
- Schilling, J.-G., Fluxes and excess temperatures of mantle plumes inferred from their interaction with migrating mid-ocean ridges, *Nature*, *352*, 397–403, 1991.
- Schilling, J.-G., R. N. Anderson, and P. Vogt, Rare earth, Fe and Ti variations along the Galápagos Spreading Center and their relationship to the Galápagos Mantle Plume, *Nature*, *261*, 108–113, 1976.
- Schilling, J.-G., M. B. Bergeron, and R. Evans, Halogens in the mantle beneath the North Atlantic, *Philos. Trans. R. Soc. London Ser. A.*, *297*, 147–178, 1980.
- Schilling, J.-G., R. H. Kingsley, and J. D. Devine, Galápagos hot spot-spreading center system, 1, Spatial petrological and geochemical variations (83°W–101°W), *J. Geophys. Res.*, *87*, 5593–5610, 1982.
- Smith, D. K., and J. R. Cann, The role of seamount volcanism in crustal construction at the Mid-Atlantic Ridge (24°–30°N), *J. Geophys. Res.*, *97*, 1645–1658, 1992.
- Smith, W. H. F., and D. T. Sandwell, Global seafloor topography from satellite altimetry and ship depth soundings, *Science*, *277*, 1957–1962, 1997.
- Toomey, D. R., E. E. E. Hooff, S. Solomon, D. James, and M. Hall, Upper mantle structure beneath the Galápagos archipelago from body wave data, *Eos Trans. AGU*, *82*(46), Fall Meet. Suppl., F1205, 2001.
- Verma, S. P., and J.-G. Schilling, Galápagos hot spot-spreading center system, 2, <sup>87</sup>Sr/<sup>86</sup>Sr and large ion lithophile element variations (85°W–101°W), *J. Geophys. Res.*, *87*, 10,838–10,856, 1982.



Verma, S. P., J.-G. Schilling, and D. G. Wagoner, Neodymium isotopic evidence for Galápagos hot spot-spreading centre system evolution, *Nature*, 306, 654–657, 1983.

White, W. M., A. R. McBirney, and R. A. Duncan, Petrology and geochemistry of the Galápagos Islands: Portrait of a pathological mantle plume, *J. Geophys. Res.*, 98, 19,533–19,563, 1993.

Wilson, D. S., and R. N. Hey, History of rift propagation and magnetization intensity for the Cocos-Nazca spreading center, *J. Geophys. Res.*, 100, 10,041–10,056, 1995.

Yale, M. M., and J. Phipps Morgan, Asthenosphere flow model of hot spot-ridge interactions: A comparison and Iceland and Kerguelen, *Earth Planet. Sci. Lett.*, 161, 45–56, 1998.